ADVANCED FUNCTIONAL MATERIALS
www.afm-journal.de



# 20.0% Efficiency Si Nano/Microstructures Based Solar Cells with Excellent Broadband Spectral Response

*Zengguang Huang, Xiaomin Song, Sihua Zhong, Haiyuan Xu, Wenxing Luo, Xudong Zhu, and Wenzhong Shen**

**Spectral response of solar cells determines the output performance of the devices. In this work, a 20.0% efficient silicon (Si) nano/microstructures (N/M-Strus) based solar cell with a standard solar wafer size of 156 × 156 mm$^2$ (pseudo-square) has been successfully fabricated, by employing the simultaneous stack $SiO_2/SiN_x$ passivation for the front N/M-Strus based $n^+$-emitter and the rear surface. The key to success lies in the excellent broadband spectral responses combining the improved short-wavelength response of the stack $SiO_2/SiN_x$ passivated Si N/M-Strus based $n^+$-emitter with the extraordinary long-wavelength response of the stack $SiO_2/SiN_x$ passivated rear reflector. Benefiting from the broadband spectral response, the highest open-circuit voltage ($V_{oc}$) and short-circuit current density ($J_{sc}$) reach up to 0.653 V and 39.0 mA cm$^{-2}$, respectively. This high-performance screen-printed Si N/M-Strus based solar cell has shown a very promising way to the commercial mass production of the Si based high-efficient solar cells.**

## 1. Introduction

Excellent broadband spectral responses are of great significance for promoting energy conversion efficiencies ($\eta$'s) of solar cells.[1] The commercial large-area silicon (Si) based solar cells have demonstrated perfect spectral response in the medium-wavelength range of 500–800 nm, while both the long-wavelength and short-wavelength spectral response is not good enough, mainly due to the large recombination loss of back surface field (BSF)[2] and the high residual reflectance at the front surface,[3] respectively. To achieve the excellent broadband spectral response of the Si based solar cells, it is necessary to further improve the optical and electrical properties of the rear surface as well as the front surface. By introducing passivation dielectric thin films at the rear surface, Green group[4] has successfully fabricated a 22.8% efficient passivated emitter and rear cell (PERC) with an area of 4 cm$^2$, manifesting superior long-wavelength spectral response due to the low recombination velocity and high long-wavelength reflectivity at the rear surface.[5] This long-wavelength superiority has been recently employed in the photovoltaic industry for the mass production of 20.0% efficient PERCs on commercial large-area (156 × 156 mm$^2$) Si wafers.[6,7]

On the other hand, Si nanostructure array provides a promising approach to enhancing the energy harvesting in the short-wavelength range, for the near zero and small-angle-dependent reflectivity in the short-wavelength region.[8–15] By employing the well short-wavelength antireflection of the Si nanostructure array, many authors have made relative progresses in the cell performances of the Si nanostructures based solar cells.[16–21] But $\eta$'s of these Si nanostructures based solar cells are still not satisfied when comparing with those of the traditional solar cells, which is mainly attributed to the large surface recombination loss from the Si nanostructures. Surface passivation such as thermal $SiO_2$,[4,11,22] $SiN_x$:H by plasma enhanced chemical vapor deposition (PECVD),[23,24] and $Al_2O_3$ by atomic layer deposition (ALD)[25–27] can effectively suppress the surface recombination by saturating the dangling bonds or forming the fixed charges at and near the surface. Particularly, the stack $SiO_2/SiN_x$ layers provide an excellent passivation for the Si nanostructures,[28–30] which benefits from the well surface passivation of the inner $SiO_2$ as well as the bulk passivation of the outer $SiN_x$:H. The simultaneous surface and bulk passivation guarantee the well electrical performance of the Si nanostructures based solar cells.

As a result, the passivated front Si nanostructures together with the passivated rear surface are able to provide the complementary spectral responses in both the short-wavelength and long-wavelength region, implying an effective way to achieve the excellent broadband spectral response of Si based solar cells. In this paper,

Dr. Z. G. Huang, Dr. S. H. Zhong, H. Y. Xu, Prof. W. Z. Shen
Laboratory of Condensed Matter Spectroscopy and Opto-Electronic Physics
and Key Laboratory of Artificial Structures and Quantum Control (Ministry of Education)
Department of Physics and Astronomy, and Institute of Solar Energy
Shanghai Jiao Tong University
Shanghai 200240, P. R. China
E-mail: wzshen@sjtu.edu.cn
Dr. Z. G. Huang, X. M. Song
School of Science
Huaihai Institute of Technology
Lianyungang 222005, P. R. China
W. X. Luo, X. D. Zhu
Nice Sun PV Co., Ltd.
Jiangsu Province, Wuxi 214233, P. R. China
Prof. W. Z. Shen
Collaborative Innovation Center of Advanced Microstructures
Nanjing 210093, P. R. China

**DOI: 10.1002/adfm.201503553**

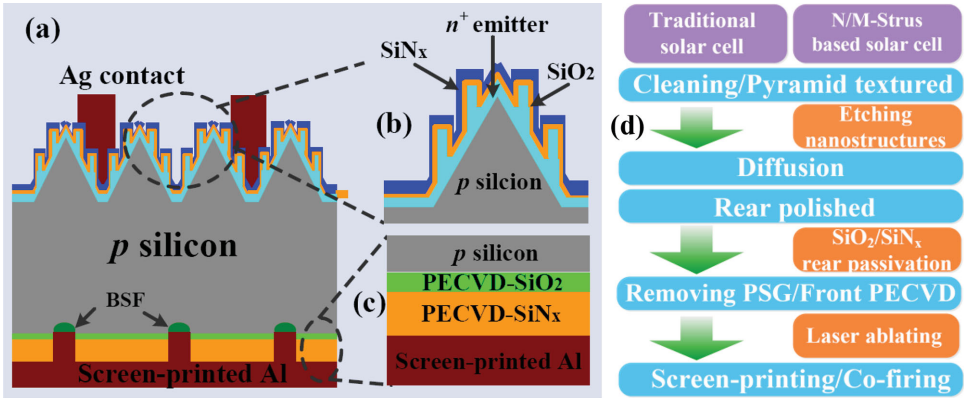


**Figure 1.** Design and process of the Si N/M-Strus based solar cell. a) The schematic diagram of Si N/M-Strus based solar cell. b) The stack $SiO_2/SiN_x$ (PECVD) passivated Si N/M-Strus based $n^+$-emitter. c) The rear reflector consisting of the stack $SiO_2/SiN_x$ (PECVD) layers and the screen-printed Al. d) The process flow of the Si N/M-Strus based solar cell comparing with that of the traditional one.

we perform the simultaneous stack $SiO_2/SiN_x$ (PECVD) passivation for the front Si nano/microstructures (N/M-Strus) and rear surface, and successfully achieve a 20.0% $\eta$ of the screen-printed Si N/M-Strus based solar cell with a standard solar wafer size of $156 \times 156$ mm$^2$. This Si N/M-Strus based solar cell possesses excellent broadband spectral response due to the improved short-wavelength response of the stack $SiO_2/SiN_x$ passivated N/M-Strus emitter and the outstanding long-wavelength response of the stack $SiO_2/SiN_x$ passivated rear surface. The proposed device structure and technique open a broad way to the mass production of Si nanostructures based solar cells.

## 2. Design of Device Structure

The device structure of Si N/M-Strus based solar cell (see **Figure 1**a) is designed as follows: (i) The Si N/M-Strus based $n^+$-emitter passivated by stack $SiO_2/SiN_x$ (PECVD) layers as shown in Figure 1b. The Si N/M-Strus possess an excellent short-wavelength antireflection effect, while the stack $SiO_2/SiN_x$ layers simultaneously provide an outstanding passivation for the surface and bulk of the Si N/M-Strus based $n^+$-emitter. The simultaneous consideration of optical and electrical performance will guarantee the well short-wavelength response. (ii) The rear reflector consists of the inner $SiO_2$ (PECVD) layer, the outer $SiN_x$ (PECVD) layer, and screen-printed Al as shown in Figure 1c. The design of the stack dielectric layers can provide more variables (thickness and refractive index) than that of single layer for optimizing the long-wavelength optical properties, while it keeps the well electrical passivation effect. This design predicts an excellent broadband spectral response from the simultaneously improved spectral responses in both short-wavelength and long-wavelength region.

## 3. Short-Wavelength Optical and Electrical Performance

**Figure 2**a is the cross-sectional view scanning electron microscopy (SEM) image of Si N/M-Strus, which clearly shows the Si nanowires (Si NWs) along with the ⟨100⟩ crystal orientation on the surface of micro-pyramid texture. We notice that the Si NWs on the top of pyramid are longer than those on the bottom of pyramid, indicating that the etching velocity of Si NWs is increasing from bottom to top. From the top view SEM image of Si N/M-Strus (see Figure 2b), the etching velocity difference between the top and bottom can also be distinguished. The varying length of Si NWs on the pyramid texture can provide a better antireflection effect, which plays a role of antireflective medium with the gradient refractive index. From the SEM images, the average length and diameter of the Si NWs are estimated as ≈80 and ≈60 nm, respectively, and the average length becomes larger with the increase of the etching time, which is consistent with our previous result.[15]

The front surface of commercial Si solar cell is commonly coated by $SiN_x$:H (PECVD) thin film, which can both reduce the front reflectance and suppress the $n^+$-emitter recombination including surface and Auger recombination.[11] As is discussed in the Introduction, the stack $SiO_2/SiN_x$ layers can provide a better surface passivation, therefore, we perform continuous deposition of $SiO_2$ and $SiN_x$ layer on the surface of the Si N/M-Strus based $n^+$-emitter in the PECVD chamber. Figure 2c displays the top view SEM image of stack $SiO_2/SiN_x$ coated Si N/M-Strus based $n^+$-emitter. The thickness of inner $SiO_2$ and the outer $SiN_x$ layer are estimated as ≈10 and ≈70 nm, respectively.

Now, we focus on the short-wavelength optical property of the stack $SiO_2/SiN_x$ coated Si N/M-Strus. Figure 2d shows the comparison of reflectance for Si N/M-Strus based solar cell and traditional solar cell, which manifests the better short-wavelength antireflection effect of Si N/M-Strus than that of the traditional one. As is discussed in our previous work,[15,20,31] the combined antireflection from the Si N/M-Strus and the stack $SiO_2/SiN_x$ layers benefits to this short-wavelength optical superiority, which is the prerequisite of obtaining good external quantum efficiencies (EQEs) in the short-wavelength range. Also, we see the higher reflectance of Si N/M-Strus in the wavelength range of 420–500 nm, which can be solved by optimizing the thickness of the outer $SiN_x$ antireflective thin film.

The electrical performance of the $n^+$-emitter has an essential effect on the short-wavelength spectral response of the solar cell. In our case, the inner ultrathin $SiO_2$ layer is able to provide an excellent surface modification by Si—O saturating the dangling

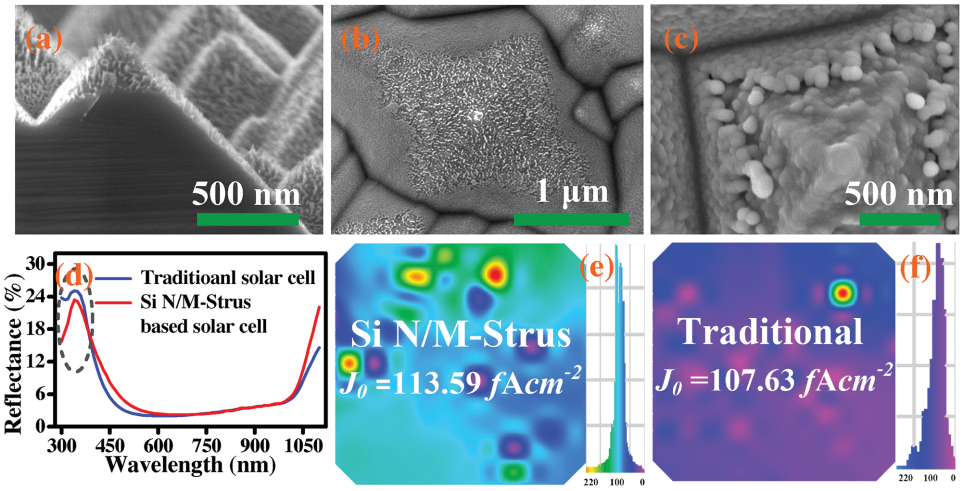


**Figure 2.** Morphological, optical, and electrical properties of the prepared Si N/M-Strus. a) The sectional-view SEM image of the Si N/M-Strus. b) The top-view SEM image of the Si N/M-Strus. c) The top-view SEM image of the stack $SiO_2/SiN_x$ (PECVD) coated Si N/M-Strus. d) The superiority of optical antireflection for the Si N/M-Strus based solar cell comparing with the traditional one. e) The $J_{0e}$ (113.59 fA cm$^{-2}$) mapping of the Si N/M-Strus based $n^+$-emitter. f) The $J_{0e}$ (107.63 fA cm$^{-2}$) mapping of the traditional pyramid-textured solar cell.

bonds at the surface of the Si N/M-Strus based $n^+$-emitter, meanwhile the outer $SiN_x$:H (PECVD) layer still keep the same bulk passivation because the H atoms can easily pass through the inner ultrathin $SiO_2$ layer. Therefore, the front stack passivation of $SiO_2/SiN_x$ can guarantee a better electrical performance of Si N/M-Strus based $n^+$-emitter, which is characterized by the saturation current density $J_{0e}$ of the $n^+$-emitter. Generally, the $J_{0e}$ of the $n^+$-emitter is determined by the following expression

$$\frac{1}{\tau_{\text{eff}}} - \frac{1}{\tau_{\text{Auger}}} = \frac{1}{\tau_{\text{SRH}}} + (J_{0e(\text{front})} + J_{0e(\text{back})}) \frac{N_A + \Delta n}{q n_i^2 d} \quad (1)$$

where $\tau_{\text{eff}}$, $\tau_{\text{Auger}}$, and $\tau_{\text{SRH}}$ are the effective, Auger recombination, and the bulk lifetime considering only the Shockley–Read–Hall (SRH) recombination, respectively, $N_A$ is the doping concentration of the p-Si substrate, $\Delta n$ is the excess carrier density, $q$ is the elementary charge, and $n_i$ is the intrinsic carrier density. Obviously, the lower $J_{0e}$ implies the smaller recombination loss of the $n^+$-emitter including the surface and Auger recombination. From the measurement of $J_{0e}$ mapping, Figure 2e gives the averaged $J_{0e}$ of the Si N/M-Strus based $n^+$-emitter passivated by the $SiO_2/SiN_x$ stack layers. Comparing with the $J_{0e}$ (107.63 fA cm$^{-2}$) of the traditional $n^+$-emitter as shown in Figure 2f, the stack passivated Si N/M-Strus based $n^+$-emitter possesses similar value of 113.59 fA cm$^{-2}$, which is far smaller than that of single $SiN_x$ passivated Si N/M-Strus based $n^+$-emitter (≈200 fA cm$^{-2}$). This proves the excellent passivation effect of the stack $SiO_2/SiN_x$, due to the effective removal of the electrical disadvantages from the large surface area of Si N/M-Strus. Moreover, the $J_{0e}$ mapping shows the relative uniformity of the diffused morphology of the Si N/M-Strus based $n^+$-emitter, although some local surfaces have the higher or lower values of $J_{0e}$ caused by the high temperature diffusion or Si NWs etching process.

To evaluate the contribution of $J_{0e}$ to the total diode saturating current density $J_0$, we calculate the $J_0$ according to the measured open-circuit voltage ($V_{oc}$) and short-circuit current density ($J_{sc}$),[7] as

$$J_0 = J_{sc} \Big/ \left[\exp\left(\frac{qV_{oc}}{kT}\right) - 1\right] \quad (2)$$

where $kT/q$ is the thermal voltage (25.693 mV at 25 °C) and $T$ is the absolute temperature. In our case, the measured values of $V_{oc}$ and $J_{sc}$ are 0.653 V and 9.484 A, respectively, so, we obtain the value of $J_0$ as 357.15 fA cm$^{-2}$. Obviously, the $J_{0e}$ with the measured 113.59 fA cm$^{-2}$ plays a secondary role in the total diode saturating current density $J_0$, implying that the post processes including the screen-printed front and back contacts yield the dominant recombination. This also means that the low $J_{0e}$ of the stack passivated $n^+$-emitter makes it feasible to further lower the total $J_0$ of the solar cell by optimizing the contact materials and processes.

As a result, the improved optical gain from the Si N/M-Strus, together with the reduced electrical loss from the excellent surface and bulk passivation of the stack $SiO_2/SiN_x$, predicts the better short-wavelength spectral response expressed by the EQEs as will be shown below.

## 4. Long-Wavelength Optical and Electrical Performance

The rear reflector consists of the inner $SiO_2$ (PECVD) layer, the outer $SiN_x$ (PECVD) layer, and the screen-printed Al, as shown in Figure 1c. From the cross-sectional view SEM image as shown in **Figure 3**b, the thicknesses of the inner $SiO_2$ and outer $SiN_x$ at the rear surface are estimated as ≈25 and ≈250 nm, respectively. High internal rear reflectance (IRR) at long-wavelength region can enhance the light absorption in the bulk Si of solar cell by reducing the light absorption in full Al-BSF and increasing the propagation path,[32] resulting in the improvement of the long-wavelength quantum efficiency (QE), i.e., long-wavelength spectral response. To better understand the IRR, it is necessary to evaluate the $R_{\text{IRR}}$ from the measured total hemisphere reflectance ($R_{\text{measure}}$)

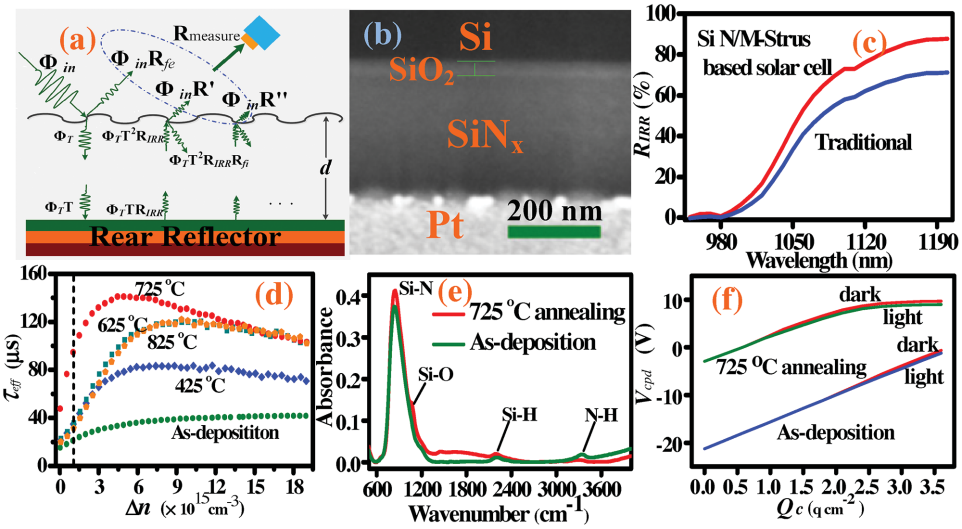


**Figure 3.** Optical and electrical performance of the rear reflector. a) The Lambertian light-trapping scheme in our case, with $R_{IRR}$ being the internal rear reflectivity. $R$, $R'$, and $R''$ are the front reflectivity corresponding to primary, secondary, and tertiary reflection, respectively. b)The cross-sectional view SEM image of the stack $SiO_2/SiN_x$ (PECVD) layers coated rear surface. c) Comparison of the long-wavelength IRR of Si N/M-Strus based solar cell with that of the traditional one. d) $\tau_{eff}$ with respect to the injection level $\Delta n$ at different annealing temperature for symmetrical stack $SiO_2/SiN_x$ passivated wafers. The dashed line denotes 1 sun injection level. e) The FTIR spectra of the 725 °C annealing sample comparing with that of the as-deposition sample. f) The coronal charge–voltage curves in the dark and light modes for the 725 °C annealing and the as-deposition sample. $V_{cpd}$ and $Q_c$ denote the contact potential difference and coronal charge density, respectively. The differences of the interface trap charges difference ($\Delta Q_{it}$) and the surface barrier voltage difference ($\Delta V_{sb}$) between light and dark modes are measured as $1.31 \times 10^{11}$ q cm$^{-2}$ and 0.271 V for the 725 °C annealing sample, as well as $4.52 \times 10^{11}$ q cm$^{-2}$ and 0.454 V for the as-deposition sample.

by employing diffusely scattering (Lambertian) model.[33,34] Figure 3a illustrates the Lambertian light-trapping scheme in our case, which is based on the front random surface Si N/M-Strus based textures and rear reflector consisting of the stack $SiO_2/SiN_x$ layers and screen-printed Al. According to the Gee's method,[33] we have the expression of the measured total hemisphere reflectance

$$R_{measure} = \frac{\Phi_{in}R_{fe} + \Phi_{in}R' + \Phi_{in}R'' + \Phi_{in}R''' + \ldots}{\Phi_{in}} = R_{fe} + R' + R'' + R''' + \ldots \quad (3)$$

$$R' = (1-R_{fe})(1-R_{fi})T^2R_{IRR} \quad (4)$$

$$R'' = (1-R_{fe})(1-R_{fi})(T^2R_{IRR})(T^2R_{IRR}R_{fi}) \quad (5)$$

$$R''' = (1-R_{fe})(1-R_{fi})(T^2R_{IRR})(T^2R_{IRR}R_{fi})^2 \quad (6)$$

where $\Phi_{in}$ and $\Phi_T$ are the incidence and transmission light flux, $R_{fe}$ and $R_{fi}$ are the external and internal reflectivity of the front surface, $T$ and $R_{IRR}$ are the bulk transmission coefficient and internal rear reflectivity, respectively. Here, $R'$, $R''$, and $R'''$ form a geometric sequence where the common radio is $T^2R_{IRR}R_{fi}$, therefore, Equation (3) can be rewritten as

$$R_{measure} = R_{fe} + \frac{(1-R_{fe})(1-R_{fi})T^2R_{IRR}}{1-T^2R_{IRR}R_{fi}} \quad (7)$$

Assuming $T = 1$ at long-wavelength range, we have

$$R_{IRR} = \frac{R_{measure} - R_{fe}}{(1-R_{fe})(1-R_{fi}) + (R_{measure} - R_{fe})R_{fi}} \quad (8)$$

where the corresponding values of $R_{fe}$ in the range of 950–1200 nm can be obtained from the linear equation which is linearly fitted from the values of $R_{measure}$ in the range of 700–950 nm. $R_{fi}$ is evaluated as a fixed value of 0.92, when the light trapping scheme is Lambertian. Figure 3c shows the internal rear reflectivity $R_{IRR}$ of Si N/M-Strus based solar cell in the long-wavelength region, comparing with that of traditional cell. Obviously, $R_{IRR}$ of the Si N/M-Strus based solar cell has greatly increased in the range of 950–1200 nm due to the stack $SiO_2/SiN_x$ layers between the bulk Si and screen-printed Al. The increases of $R_{IRR}$ bring about two results: (i) The increasing long-wavelength absorption in bulk Si. (ii) The increasing long-wavelength $R_{measure}$ as shown in Figure 2d. It is undoubted that the former is beneficial to the long-wavelength spectral response of Si N/M-Strus based solar cell.

To show the electrical superiority of the stack $SiO_2/SiN_x$ layers, we in this section investigate the influence of the different annealing conditions on the effective minority carrier lifetime ($\tau_{eff}$) with respect to the injection level ($\Delta n$), as shown in Figure 3d. Notice that all the polished Si wafers have the same bulk minority carrier lifetime of ≈200 μs, and then the stack $SiO_2/SiN_x$ layers are symmetrically deposited on both sides of polished Si wafers. We perform four annealing conditions as 425, 625, 725, and 825 °C for 5 min in the air atmosphere. We notice that the 22 μs $\tau_{eff}$ of the as-deposited $SiO_2/SiN_x$ passivated sample at the injection density of $1.2 \times 10^{15}$ cm$^{-3}$ (1 sun injection level) is obviously higher than the ≈15 μs $\tau_{eff}$ of the single $SiN_x$ layer passivated Si wafer, demonstrating the

excellent surface modification ability of the inner $SiO_2$ layer. Importantly, when the samples undergo an annealing process in the air atmosphere, the values of $\tau_{eff}$ have greatly increased compared with that of the as-deposition sample. With the increase of annealing temperature from 425 to 725 °C, the $\tau_{eff}$ increases and reaches the highest value of 142 μs ($\Delta n$ = $4.9 \times 10^{15}$ $cm^{-3}$) at 725 °C. According to the Equation (1) $1/\tau_{eff} = 1/\tau_{bulk} + 2S_{eff}/d$, the surface recombination velocity (SRV) of the symmetrical stack $SiO_2/SiN_x$ passivated Si wafer after annealing at 725 °C can be calculated as an ultra-low value of 18.3 cm $s^{-1}$, which manifests an extraordinary passivation effect for a solar-grade p-type Si wafer. When the annealing temperature further increases to 825 °C, the values of the $\tau_{eff}$ display a declining trend. It is worth noticing that the optimized annealing process is close to the co-firing process of solar cell, i.e., the annealing process can be combined with the co-firing process.

To further understand the influence of the annealing process on the surface modification, we compare the Fourier transform infrared spectroscopic (FTIR) absorption spectra of the optimized annealing-process sample (725 °C) with that of the as-deposition sample. Figure 3e manifests that the Si—N, Si—O, Si—H, and N—H bonds correspond to the stretching absorption peaks at the wavenumbers of ≈840, 1070, 2200, and 3340 $cm^{-1}$, respectively. We see that the densities of both the Si—N and Si—O bonds show an obvious increase after annealing at 725 °C, meanwhile the density of the Si—H bonds increases slightly. The increases of the Si—O and Si—H bonds density imply the decrease of the dangling bonds at the interface of $Si/SiO_2$, resulting in a better passivation effect.[35] Also, the annealing process promotes the density of Si—N bonds, indicating a more dense structure which can effectively prevent the out diffusion of H from entering into the environment instead of into Si bulk. However, for an excessively high annealing temperature, the H in Si—H and N—H groups can escape from the bulk Si and the dielectric layers to the environment, which causes the decline of the passivation effect.[35]

Also, the improvement of the surface passivation after annealing is quantitatively reflected by the lower value of interface trap density $D_{it}$. From corona charge–voltage curves, the interface trap density $D_{it}$ is calculated according to the equation of $D_{it} = \Delta Q_{it}/\Delta V_{sb}$ with $\Delta Q_{it}$ and $\Delta V_{sb}$ being the differences of the interface trap charges and surface barrier voltage between light and dark modes, respectively. As shown in Figure 3f, we obtain that the $D_{it}$ of the 725 °C annealing and as-deposition samples are $4.85 \times 10^{11}$ and $9.92 \times 10^{11}$ $cm^{-2}$ $eV^{-1}$, respectively. This demonstrates that the annealing process can effectively reduce the $D_{it}$ from increasing the Si—O and Si—H bonds at the interface of $Si/SiO_2$, in good agreement with the result of the FTIR measurement.

## 5. Broadband Spectral Response of Si N/M-Strus Based Solar Cell

Based on the excellent optical and electrical performance of the simultaneous stack $SiO_2/SiN_x$ layers passivated front emitter and rear reflector, we fabricate the Si N/M-Strus based solar cells. To illustrate the superior broadband spectral response, we compare the reflectance, internal QE (IQE) and EQE of the Si N/M-Strus based solar cell with those of the traditional solar cell, as shown in **Figure 4**a,b. First, in the short-wavelength range, the optical reflectance has been greatly suppressed by the Si N/M-Strus, while the corresponding IQEs of the Si N/M-Strus based solar cell show a declining trend due to the larger surface recombination of the Si N/M-Strus. Through the optimized Si N/M-Strus morphology as discussed in our previous paper,[21] we achieve that the short-wavelength optical gain overcomes the electrical loss of the front emitter, i.e., an improvement of the EQEs in the short-wavelength range. From Figure 4b, the short-wavelength EQEs of the Si N/M-Strus based solar cell are clearly better than those of the traditional solar cell. The medium-wavelength EQEs have shown a slight declining trend, which will be optimized in the future work by matching the thickness of the front stack $SiO_2/SiN_x$ with the Si N/M-Strus.[20] Second, Figure 4a shows that both the long-wavelength IRR and IQEs of the Si N/M-Strus based solar cell are superior to that of traditional solar cell, and thus the long-wavelength EQEs of the Si N/M-Strus based solar cell possess great superiority as shown in Figure 4b.

**Table 1** lists the performances of Si N/M-Strus based solar cells, as well as the traditional counterparts. Obviously, the cell performance of Si N/M-Strus based solar cell greatly surpasses that of the traditional one, which is attributed to its excellent broadband spectral response. First, comparing with the $I_{sc}$ (9.064 A) of the traditional solar cell, the average $I_{sc}$ of the Si N/M-Strus based solar cells is much higher with an absolute increment of 0.246 A, reaching 9.310 A, due to the improved front short-wavelength antireflection and the back long-wavelength IRR. Second, the average $V_{oc}$ of Si N/M-Strus based solar cells demonstrates a high value of 0.649 V which is higher by an absolute 10 mV than that of the traditional one, and the highest $V_{oc}$ reaches up to the value of 0.653 V. This demonstrates that the simultaneous passivation for the front and rear surface by the stack $SiO_2/SiN_x$ have greatly suppressed the electrical recombination loss at both sides of the cell. Finally, based on the great increases of high $I_{sc}$ and $V_{oc}$, we have successfully achieved the high-performance Si N/M-Strus based solar cells with an average $\eta$ of toward-20.0%. The highest $\eta$ of 20.0% with the $V_{oc}$ of 0.653 V and $I_{sc}$ of 9.484 A, is confirmed by the TÜV Rheinland Co., Ltd (see Figure 4c). Figure 4d is photograph of the front and rear surface of the Si N/M-Strus based solar cell.

## 6. Conclusions

In conclusion, we propose the structure of the simultaneously passivated Si N/M-Strus based $n^+$-emitter and rear surface, and successfully fabricate the high-performance Si N/M-Strus based solar cell with a large area of $156 \times 156$ $mm^2$ by using the process compatible with the current commercial solar cells. By performing the simultaneous stack $SiO_2/SiN_x$ passivation for the Si N/M-Strus based $n^+$-emitter and rear surface, we find that the simultaneous passivation guarantees the better short-wavelength antireflection, the effective suppression of the front emitter recombination ($J_{0e}$ = 113.59 fA $cm^{-2}$), the higher long-wavelength $R_{IRR}$ of rear reflector and the ultra-low SRV (18.3 cm $s^{-1}$) of the rear surface. Benefiting from the simultaneous improved performance at the front Si N/M-Strus based

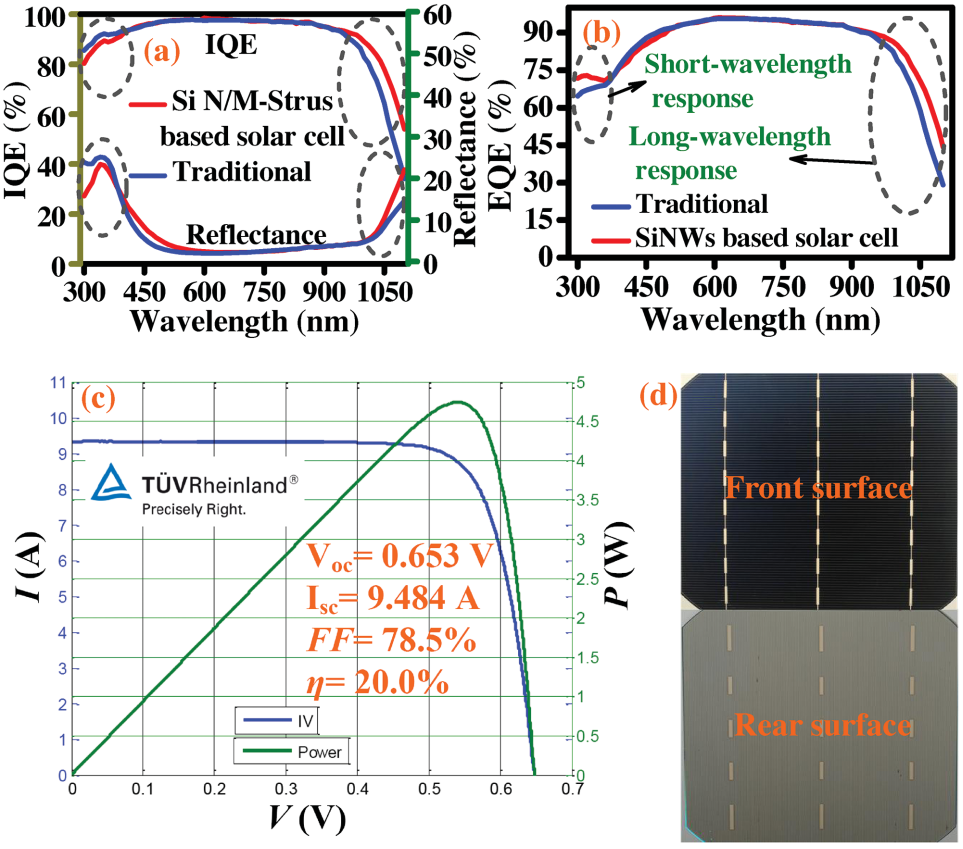


**Figure 4.** The broadband spectral response of the 20.0% efficient Si N/M-Strus based solar cell. a) The IQE and reflectance of the Si N/M-Strus based solar cell, comparing with those of the traditional one. b) The EQE of the Si N/M-Strus based solar cell, comparing with those of the traditional one. c) The *I*–*V* curve of the highest 20.0% efficient Si N/M-Strus based solar cell confirmed by the TÜV Rheinland Co., Ltd. d) Photograph of the Si N/M-Strus based solar cell.

**Table 1.** Cell performance of the Si N/M-Strus based solar cell, comparing with that of the traditional solar cell.

| Cell (156 × 156 mm$^2$) | | Output parameters | | | |
|---|---|---|---|---|---|
| | | $I_{sc}$ [A] | $V_{oc}$ [V] | FF [%] | $\eta$ [%] |
| Si N/M-Strus based solar cell | Average | 9.310 | 0.649 | 79.65 | 19.8 |
| | Best | 9.484 | 0.653 | 78.50 | 20.0 |
| Traditional solar cell | Average | 9.064 | 0.639 | 80.16 | 19.1 |
| | Best | 9.063 | 0.641 | 80.33 | 19.2 |

$n^+$-emitter and rear reflector, this solar cell possesses superior broadband spectral response in both the short and long-wavelength region, which is expressed as the higher EQEs in both regions. Finally, we achieve the highest $\eta$ of 20.0%, as well as the open-circuit voltage $V_{oc}$ of 0.653 V and short-circuit current $I_{sc}$ of 9.484 A ($J_{sc}$ = 39.0 mA cm$^{-2}$).

## 7. Experimental Section

Solar-grade p-type (100) Czochralski-Si (Cz-Si) pseudo-square 156 × 156 mm$^2$ wafers were used with 2 Ω cm resistivity and 190 ± 10 μm thickness. Figure 1d shows the process flow of the Si N/M-Strus based solar cell comparing with that of the traditional pyramid-textured solar cell. After the standard cleaning process and 80 °C-NaOH-etching pyramid-textured process, the traditional $n^+$-emitter was formed on the front surface of wafer by $POCl_3$ diffusion in a quartz-tube furnace for 40 min at 800 °C (M5111-4WL/UM, CETC 48th Research Institute). On the other hand, by the one-step metal-assisted chemical etching (MACE), the Si nanostructures were etched on the pyramid texture in the mixed solution of HF (4 M)/$AgNO_3$ (0.05 M) for a certain time, and then the Si N/M-Strus based $n^+$-emitter was formed by the same diffusion process with that of traditional wafer. The sheet resistances of Si N/M-Strus based $n^+$-emitter and traditional $n^+$-emitter are 85–87 Ω sq$^{-1}$. After the rear surface polishing, the stack $SiO_2/SiN_x$ passivation layers were deposited on the rear surface of Si N/M-Strus based wafer by PECVD (M82200-6/UM, CETC 48th Research Institute) for ≈60 min at 450 °C. After removing the phosphorous silicate glass (PSG) in dilute HF solutions, the deposition of the stack $SiO_2/SiN_x$ antireflective layers were performed on the front surface of the Si N/M-Strus based wafer together with the traditional one for ≈40 min at 400 °C by PECVD. The PECVD-$SiO_2$ and PECVD-$SiN_x$ layers were formed by the reaction of the NO/$SiH_4$ and $NH_4$/$SiH_4$, respectively. Subsequently, the rear stack passivation layers of Si N/M-Strus based wafer were locally ablated by a 532 nm wavelength and 10 ps pulse length laser (DR-LA-Y40, DR Laser), in order to form the 50 μm width and 1 mm pitch local line openings. Finally, the Si N/M-Strus based solar cell and traditional solar cell underwent the same commercial screen-printing (PV1200, DEK) and co-firing process (CF-Series, Despatch), to form well Ohmic contacts and local BSFs.

The morphologies of the Si N/M-Strus were investigated by field emission SEM (Ultra Plus, Zeiss). The effective minority carrier

lifetimes and the mapping saturation current density of the emitter were obtained by microwave photo-conductance decay method (WT-1200A SEMILAB) and quasi-steady-state microwave photo-conductance decay method (PV2000, SEMILAB), respectively. The absorption spectra were determined by FTIR (Nexus 870, Nicolet). The interface trap density $D_{it}$ was obtained from the curve of coronal charge–voltage (PV2000, SEMILAB). The reflectance spectra as well as the IQEs and EQEs were measured on the platform of quantum efficiency measurement (QEX10, PV Measurements). The electrical parameters of the solar cells were investigated by current–voltage ($I$–$V$) measurement under the illumination of AM 1.5 (Y05-1/UM, CETC 48th Research Institute). The performance of the N/M-Strus based solar cell with the highest $\eta$ was independently certified by the TÜV Rheinland (Shanghai) Co., Ltd.

## Acknowledgements

This work was supported by the Natural Science Foundation of China (61234005, 11474201, and 11174202), the Shanghai Municipal Project (14DZ1201000), the Natural Science Foundation of Jiangsu Province (BK20151284 and BK20140448), and the Innovation Foundation of HHIT (Z2014018).

Received: August 22, 2015
Revised: November 21, 2015
Published online: February 8, 2016

[1] M. A. Green, *Prog. Photovolt.: Res. Appl.* **2009**, *17*, 183.
[2] A. Aberle, W. Warta, J. Knobloch, B. Voss, *Twenty First IEEE Photovoltaic Specialists Conf.* **1990**, *1*, 233.
[3] F. Toor, H. M. Branz, M. R. Page, K. M. Jones, H. C. Yuan, *Appl. Phys. Lett.* **2011**, *99*, 103501.
[4] A. W. Blakers, A. Wang, A. M. Milne, J. Zhao, M. A. Green, *Appl. Phys. Lett.* **1989**, *55*, 1363.
[5] Z. Wang, P. Han, H. Lu, H. Qian, L. Chen, Q. Meng, N. Tang, F. Gao, Y. Jiang, J. Wu, W. Wu, H. Zhu, J. Ji, Z. Shi, A. Sugianto, L. Mai, B. Hallam, S. Wenham, *Prog. Photovolt.: Res. Appl.* **2012**, *20*, 260.
[6] T. Dullweber, S. Gatz, H. Hannebauer, T. Falcon, R. Hesse, J. Schmidt, R. Brendel, *Prog. Photovolt.: Res. Appl.* **2012**, *20*, 630.
[7] M. A. Green, *Sol. Energy Mater. Sol. Cells* **2015**, *143*, 190.
[8] K. Q. Peng, Y. Xu, Y. Wu, Y. J. Yan, S. T. Lee, J. Zhu, *Small* **2005**, *1*, 1062.
[9] S. Koynov, M. S. Brandt, M. Stutzmann, *Appl. Phys. Lett.* **2006**, *88*, 203107.
[10] Q. K. Shu, J. Q. Wei, K. L. Wang, D. H. Wu, *Nano Lett.* **2009**, *9*, 4338.
[11] H. C. Yuan, V. E. Yost, M. R. Page, P. Stradins, D. L. Meier, H. M. Branz, *Appl. Phys. Lett.* **2009**, *95*, 123501.
[12] H. M. Branz, V. E. Yost, S. Ward, K. M. Jones, B. To, P. Stradins, *Appl. Phys. Lett.* **2009**, *94*, 231121.
[13] B. K. Nayak, V. V. Iyengar, M. C. Gupta, *Prog. Photovolt.: Res. Appl.* **2011**, *19*, 631.
[14] H. J. Syu, S. C. Shiu, Y. J. Hung, C. C. Hsueh, T. C. Lin, T. Subramani, S. L. Lee, C. F. Lin, *Prog. Photovolt.: Res. Appl.* **2013**, *21*, 1400.
[15] Z. G. Huang, S. H. Zhong, X. Hua, X. X. Lin, X. Y. Kong, N. Dai, W. Z. Shen, *Prog. Photovolt.: Res. Appl.* **2015**, *23*, 964.
[16] X. G. Liu, P. R. Coxon, M. Peters, B. Hoex, J. M. Cole, D. J. Fray, *Energy Environ. Sci.* **2014**, *7*, 3223.
[17] J. Oh, H. C. Yuan, H. M. Branz, *Nat. Nanotechnol.* **2012**, *7*, 743.
[18] S. Y. Liu, X. W. Niu, W. Shan, W. Lu, J. Y. Zheng, Y. F. Li, H. B. Duan, W. J. Quan, W. Z. Han, C. R. Wronski, D. R. Yang, *Sol. Energy Mater. Sol. Cells* **2014**, *127*, 21.
[19] X. Ye, S. Zou, K. Chen, J. Li, J. Huang, F. Cao, X. Wang, L. Zhang, X. Wang, M. Shen, X. Su, *Adv. Funct. Mater.* **2014**, *24*, 6708.
[20] S. H. Zhong, Y. Zeng, Z. G. Huang, W. Z. Shen, *Sci. Rep.* **2015**, *5*, 8915.
[21] S. H. Zhong, Z. G. Huang, X. X. Lin, Y. Zeng, Y. C. Ma, W. Z. Shen, *Adv. Mater.* **2015**, *27*, 555.
[22] R. Woehl, J. Krause, F. Granek, D. Biro, *IEEE Electron Device Lett.* **2011**, *32*, 345.
[23] C. Leguijt, P. Lölgen, J. A. Eikelboom, A. W. Weeber, F. M. Schuurmans, W. C. Sinke, P. F. A. Alkemade, P. M. Sarro, C. H. M. Marée, L. A. Verhoef, *Sol. Energy Mater. Sol. Cells* **1996**, *40*, 297.
[24] T. Lauinger, J. Schmidt, A. G. Aberle, R. Hezel, *Appl. Phys. Lett.* **1996**, *68*, 1232.
[25] J. Schmidt, A. Merkle, R. Brendel, B. Hoex, M. C. M. Van de Sanden, W. W. M. Kessels, *Prog. Photovolt.: Res. Appl.* **2008**, *16*, 461.
[26] N. M. Terlinden, G. Dingemans, M. C. M. Van de Sanden, W. M. M. Kessels, *Appl. Phys. Lett.* **2010**, *96*, 112101.
[27] B. Vermang, H. Goverde, L. Tous, A. Lorenz, P. Choulat, J. Horzel, J. John, J. Poortmans, R. Mertens, *Prog. Photovolt.: Res. Appl.* **2012**, *20*, 269.
[28] S. Q. Xiao, S. Y. Xu, *Crit. Rev. Solid State Mater. Sci.* **2014**, *39*, 277.
[29] X. X. Lin, X. Hua, Z. G. Huang, W. Z. Shen, *Nanotechnology* **2012**, *24*, 235402.
[30] Y. P. Liu, T. Lai, H. L. Li, Y. Wang, Z. X. Mei, H. L. Liang, Z. L. Li, F. M. Zhang, W. J. Wang, A. Y. Kuznetsov, X. L. Du, *Small* **2012**, *8*, 1392.
[31] Z. G. Huang, X. X. Lin, Y. Zeng, S. H. Zhong, X. M. Song, C. Liu, X. Yuan, W. Z. Shen, *Sol. Energy Mater. Sol. Cells* **2015**, *143*, 302.
[32] M. A. Green, *Prog. Photovolt.: Res. Appl.* **2002**, *10*, 235.
[33] J. M. Gee, *Twentieth IEEE Photovoltaic Specialists Conf.* **1988**, *1*, 549.
[34] A. Ristow, M. M. Hilali, A. Ebong, A. Rohatgi, presented at *17th Eur. Photovoltaic Solar Energy Conf. Exhibition*, Munich, Germany, October **2001**.
[35] G. Choi, N. Balaji, C. Park, J. Choi, S. Lee, J. Kim, M. Ju, Y. Lee, J. Yi, *Vacuum* **2014**, *101*, 22.